www.editada.org

International Journal of Combinatorial Optimization Problems and Informatics, 17(4), 2026, 74-93. ISSN: 2007-1558.
https://doi.org/10.61467/2007.1558.2026.v17i4.1295

Genetic algorithm-based optimization of CFD virtual test environments for axial cooling fan characteristic curves

Angel Ehécatl García Martínez[1], José Gustavo Leyva Retureta[1], Fernando Aldana Franco[1], Alam Josué Reyes López[1], Virginia Lagunes Barradas[2],

[1] Universidad Veracruzana, Facultad de Ingeniería Mecánica y Eléctrica Region Xalapa,
[2] Instituto Tecnológico Superior de Xalapa (ITSX), Ingeniería en Sistemas Computacionales.,
✉Corresponding author: angelehecatlgarciamartinez@gmail.com

Abstract. This study proposes a robust methodology for the efficient design of axial fans in computational cooling systems, combining Computational Fluid Dynamics (CFD) with Genetic Algorithms (GA). The objective was to design and optimize a virtual wind tunnel using SolidWorks Flow Simulation and the modified Lam-Bremhorst k-ε turbulence model. Using GAs, the tunnel's dimensional parameters (diameter, length, sensor spacing) were optimized to minimize the error with respect to manufacturer curves. The simulation of a commercial fan demonstrated that the optimized tunnel adjusted the maximum static pressure and volumetric flow values, reducing the errors (RMSE) to 1.7% and 9.2%, respectively. The methodology proved to be scalable, highlighting that the aerodynamic profile of the blades significantly influences the accuracy of the simulation of the characteristic curves with respect to the curve provided by the manufacturer.
Keywords: Genetic algorithms; CFD; characteristic curve; geometric optimization; wind tunnels; axial fans.

Article information

Received: Jan 11, 2026
Accepted: May 19, 2026

1 Introduction

The virtual wind tunnel design aims to solve a fundamental problem in the aerodynamic characterization of fans for electronics: reliably obtaining the pressure-flow characteristic curve (P-Q) without an AMCA 210 experimental bench, which is expensive to build and requires specialized infrastructure. In conventional CFD simulation, the P–Q curve often presents significant errors compared to the manufacturer-certified curve. This occurs because the geometry of the simulation domain is adopted as a standard or arbitrary value and is not calibrated for the specific fan.

Efficiency in the design and selection of axial fans is highly relevant in thermal engineering, especially in computer cooling systems. In applications such as computer cooling systems, where fans are used to optimize heat transfer, it is crucial to know their aerodynamic behavior through their characteristic curve. This curve allows evaluating the suitability of a fan for different applications and also influences the energy efficiency and durability of the associated electronic components (Zhang et al., 2019); Zhou et al., 2023). However, access to specialized test laboratories for obtaining characteristic curves can be costly and limiting, which underlines the importance of developing alternative methods based on virtual simulations.

Historically, the study of axial fans has evolved from traditional experimental methodologies to hybrid approaches combining numerical simulation and algorithmic optimization. Recent advances in artificial intelligence and evolutionary optimization have significantly expanded the use of data-driven methods for analyzing and reconstructing fan characteristic curves. For example, Liu et al. (2023) combined deep neural networks (DNN) with evolutionary optimization methods to generate pressure–flow (P–Q) curves of axial fans based on geometric design parameters, using wind tunnel data to calibrate and reduce experimental costs.

Similarly, (Zhang et al., 2019) applied an artificial neural network coupled with a genetic algorithm to optimize the volumetric flow rate of an axial fan. Their methodology demonstrated that evolutionary optimization combined with surrogate modeling can significantly reduce computational cost while maintaining predictive accuracy. This reinforces the potential of hybrid CFD–AI frameworks in fan performance prediction and aerodynamic optimization. In centrifugal and radial fan applications, Fritsche & Epple (2025) developed AI-based metamodels trained on CFD results to reconstruct complete pressure–flow curves from a limited set of geometric inputs.

In addition, machine learning techniques have been applied to operational state classification and instability detection in axial fans. Kumar et al. (2022) used clustering and neural networks to classify operating regimes based on unsteady pressure signals, identifying stall-prone regions along the characteristic curve. Liu et al. (2023) implemented gradient-based mass-flow control methods coupled with CFD to automatically generate full P–Q curves through algorithmic sweeping of operating points. Despite these advances, existing literature primarily focuses on optimizing blade geometry or constructing surrogate models to predict performance curves. To the authors' knowledge, the geometric optimization of the virtual wind tunnel as a calibration system remains an underexplored area in the context of low-pressure axial PC fan simulations.

hese contributions have shown that advanced computational techniques can significantly reduce costs and time in the design and evaluation of aerodynamic components without compromising accuracy. However, the accuracy of the simulated curves still depends on multiple factors, including wind tunnel geometry and turbulence models. This poses new challenges for researchers. In this context, the problem of optimizing the dimensions and configurations of a virtual wind tunnel to obtain accurate and reliable characteristic curves arises. Is it possible to develop a virtual wind tunnel optimized by genetic algorithms to accurately simulate PC axial fan characteristic curves? Can it fit the experimental data and reduce the margin of error to less than 10%? The resolution of this question is fundamental to establishing a replicable and efficient method that facilitates fan design and evaluation before manufacturing and contributes to the advancement of computational and thermal engineering.

The need for geometric adjustment using genetic algorithms arises because the geometry of a simulated wind tunnel determines the shape of the pressure-flow curve obtained by CFD. Previous studies focus solely on optimizing using CFD (Ahmed & Eljack, 2014) (Zhou et al., 2023). However, their results show that small variations in duct diameter, straight section length, or sensor location can significantly alter the slope and maximum value of the results. The main objective of this study is to optimize the geometric parameters of a virtual CFD test environment using a genetic algorithm to minimize the deviation between simulated and manufacturer pressure–flow curves. The aim is to evaluate the influence of key geometrical parameters on the accuracy of the simulated characteristic curves and to compare the results with experimental and theoretical data. Additionally, this work proposes to demonstrate the feasibility of this approach as a cost-reduction tool in fan design. It also aims to open new research lines in the development of aerodynamic devices.

2 Theoretical and Computational Framework

This article presents an alternative proposal for calculating the performance curve of a fan using CFD. The objective is to design a virtual wind tunnel that allows obtaining characteristic curves as faithful as possible to real fan results without requiring a high budget. This would allow designing fans and calculating their approximate performance before production, saving time and resources and optimizing fan design for different applications.

2.1 Turbulence Model

The prototype was designed with distinct inlet and outlet sections. The air inlet side would have an inlet flow rate for the fan, while the tunnel outlet would be open to the atmosphere. SOLIDWORKS Flow Simulation software was used for this work. It includes two turbulence models for fluid dynamics modeling:
IL model: This is a basic turbulence model that requires less computational effort compared to others. It considers the turbulence intensity I_T and turbulence length L_T in an approximate way to solve the turbulence equations:

$$k = \frac{3}{2}(|U|I_T)^2 \quad \textbf{(1)}$$

$$\varepsilon = C_\mu^{3/4}\frac{k^{3/2}}{L_T} \quad \textbf{(2)}$$

Flow Simulation uses a turbulence length scale based on mixing length, which differs from other codes. It is common to approximate the values of turbulence intensity and turbulence length. A value of $I_T = 0.1$ % is very low, since wind tunnels can produce values down to 0.05 %, while fully turbulent flows are kept in a range of $5\% \leq I_T \leq 10\%$. The turbulence length is approximated accordingly.

$k - \varepsilon$ model: It is a model based on derivations from other models and empirical considerations. The kinetic energy k is derived from an exact equation, while the dissipation rate ε is defined using physical reasoning. This introduces a modified transport equation derived from an exact equation for fluctuation transport and mean vorticity. The modified version made by Lam and Bremhorst describes laminar, turbulent, and transient flows of homogeneous fluids. It consists of the following turbulence conservation laws:

$$\frac{\partial \rho k}{\partial t} + \frac{\partial \rho k u_i}{\partial x_i} = \frac{\partial}{\partial x_i} + \left(\left(\mu + \frac{\mu_t}{\sigma_k} \right) \frac{\partial k}{\partial x_i} \right) + \tau_{ij}^R \frac{\partial u_i}{\partial x_j} - \rho\varepsilon + \mu_t P_B \tag{3}$$

$$\frac{\partial \rho \varepsilon}{\partial t} + \frac{\partial \rho \varepsilon u_i}{\partial x_i} = \frac{\partial}{\partial x_i} + \left(\left(\mu + \frac{\mu_t}{\sigma_\varepsilon} \right) \frac{\partial \varepsilon}{\partial x_i} \right) + C_{\varepsilon 1} \frac{\varepsilon}{k} \left(f_1 \tau_{ij}^R \frac{\partial u_i}{\partial x_j} + C_B \mu_t P_B \right) - f_2 C_{\varepsilon 2} \frac{\rho \varepsilon^2}{k} \tag{4}$$

In Lam and Bremhorst's version, damping functions are added, expressed as:

$$f_\mu = (1 - e^{-0.025 R_y})^2 \left(1 + \frac{20.5}{R_t} \right), f_1 = 1 + \left(\frac{0.05}{f_\mu} \right)^3 \tag{5}$$

and $f_2 = 1 - e^{R_t^2}$ which decrease the turbulent viscosity and turbulence energy while increasing the turbulence dissipation when the critical Reynolds number largely decreases.

The turbulence model constants are internally defined by the CFD solver according to the standard k–ε formulation. The user does not modify these coefficients directly. Instead, the simulation is driven by experimentally measurable parameters such as inlet velocity, rotational speed, pressure boundary conditions, and fluid properties.

The Reynolds stress tensor $\tau_{ij}^R = -\rho \overline{u_i' u_j'}$ is modeled using the Boussinesq approximation. Launder & Spalding (1974) were the first to establish the constants used in this work and in all those that use this model, the standard k–ε constants used in this work are $C_{\varepsilon 1} = 1.40 - 1.50$, $C_{\varepsilon 2} = 1.80 - 2.00$, $\sigma_k = 0.85 - 1.10$, $\sigma_\varepsilon = 1.2 - 1.4$, and $C_\mu = 0.07 - 0.10$. For buoyancy-driven flows, C_B is set within the range 0–1 depending on thermal effects. The turbulence closure is handled internally by SolidWorks Flow Simulation using a standard k–ε RANS formulation. The model constants are predefined and not user-adjustable, ensuring numerical stability and consistency with validated industrial practices. While the coefficients are not directly modified, they govern the turbulent viscosity field, which significantly influences wake development, boundary layer growth, and aerodynamic losses inside the wind tunnel domain. Therefore, although experimental parameters define the boundary conditions, the turbulence model plays a fundamental role in determining the predicted P–Q characteristic curves of the axial fan.

In general, the $k - \varepsilon$ model is the best known in the category of two-equation models due to its time saving and accuracy for a wide variety of scenarios as it has different versions.

Since the $k - \varepsilon$ model provides a higher quality simulation in Flow Simulation compared to the IL model, it was decided to take this model for the results of the simulations. However, a comparison between the results obtained with both models is shown below.

3 Methodology

The methodological strategy of this study is structured as a sequential calibration–optimization pipeline in which the virtual wind tunnel is treated as an adjustable geometric system. The objective is not to redesign the fan blades, but to minimize the discrepancy between CFD-generated characteristic curves and certified manufacturer data by optimizing the geometry of the computational domain (Fig. 1).

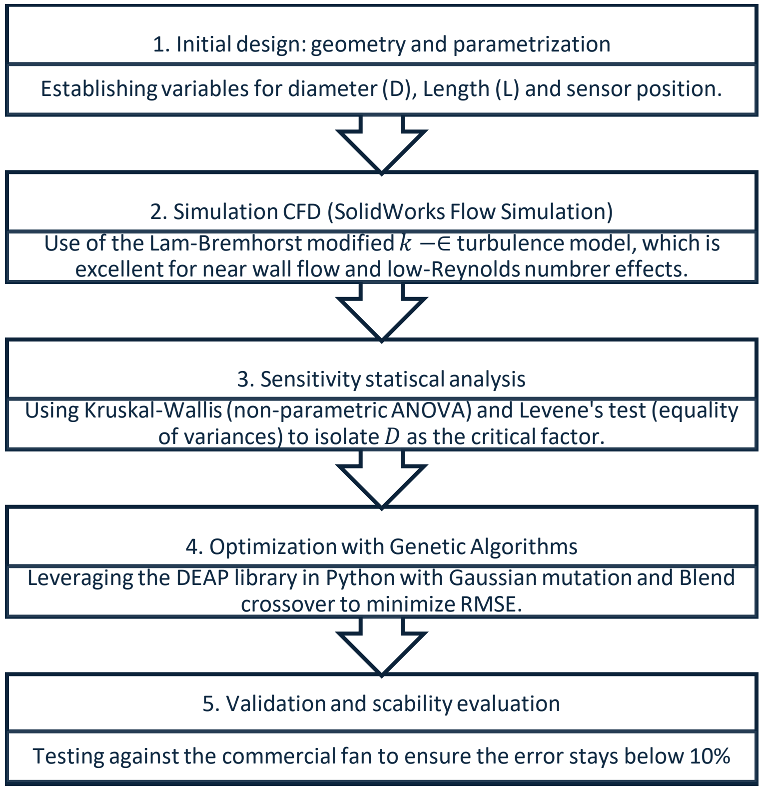

Fig. 1. Methodology used in the study.

3.1 Initial Design: Geometry and Parameterization

The surfaces used to simulate the theoretical curve were located at the center of the tunnel in a symmetrical way. The first curve simulated corresponded to the EBM W4S200HH0401 fan, which operates at 1348 rpm and has a diameter of 198 mm. The separation between the air suction and expulsion faces is 80 mm. This distance represents the fan thickness in question and was varied for each fan model subsequently simulated. The result of the design is shown in Figure 2:

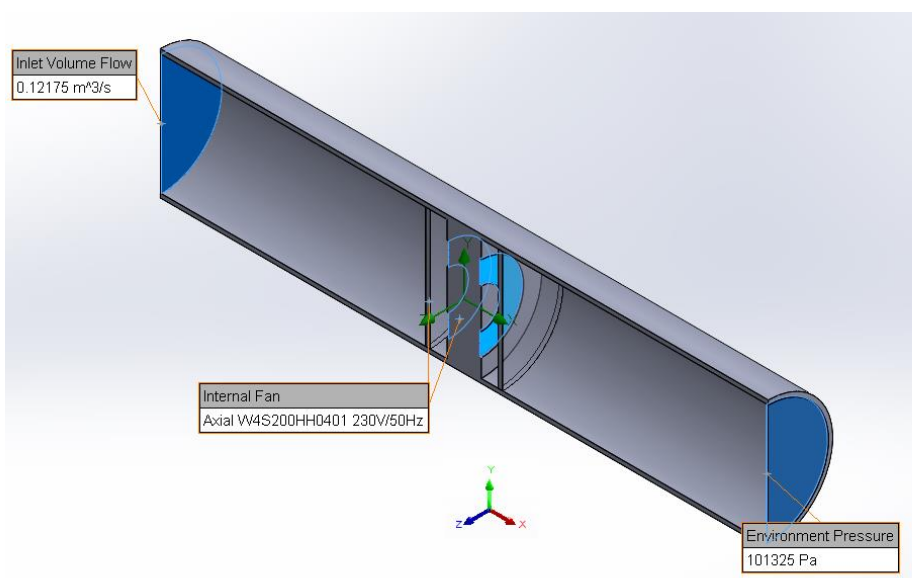

Fig. 2. Initial wind tunnel to simulate characteristic curves.

The dimensions considered in the tunnel design were:

- Tunnel diameter (D)
- Tunnel length (L)
- Sensor position (S)

These parameters were selected because they influence confinement effects, pressure recovery development, and measurement stability in ducted axial fan simulations. The parameters were defined within proportional ranges relative to the fan diameter to preserve geometric similarity and avoid unrealistic configurations. The goal at this stage was not optimization but controlled variation for sensitivity analysis. A duct diameter that is too close to the fan diameter causes significant blockage: the impeller wake occupies almost the entire section, wall effects intensify losses, and velocity distribution becomes highly non-uniform. This tends to overestimate the pressure drop and distort the shape of the P–Q curve. Conversely, excessively large diameters produce regions of dead flow and recirculation far from the area of interest, which artificially smooths the pressure gradients.

The length of the tunnel determines the flow development. If the straight downstream section is too short, the flow does not have time to stabilize and the pressure field in the measuring section continues to be affected by acceleration zones, edge effects, etc. Very long lengths, on the other hand, add unnecessary losses and can shift the entire curve without providing additional physical information.

The wind tunnel length was selected by simulating different lengths until no significant changes in pressure differences ($\Delta P < 0.001$) or return currents were observed. This methodology was also applied to determine sensors location. Simulations were performed for different inlet flow rates, and the static pressure differences between the fan inlet and outlet sensors were calculated. These values were used to plot the characteristic curve.

The position of the sensors defines in which region of the flow field the magnitudes that are compared with the reference curve are measured. If the measuring surfaces are too close to the fan, they are influenced by the rotational field, the non-uniformity of the wake, and local three-dimensional effects. If they are too far away, the signal is filtered by distributed losses and possible recirculation.

These dimensions were varied within a defined range to observe their effect on the results, and equations with different proportionality constants were formulated. These equations are:
To calculate the internal diameter of the tunnel:

$$Duct = C * Dvent \tag{6}$$

For the total length of the tunnel:

$$Length = C * Dvent \tag{7}$$

For the distance at which each sensor would be placed with respect to the fan:

$$Sensor = \frac{Dvent}{C} \tag{8}$$

Where $Dvent$ is the fan diameter and C is the proportionality constant. Through experimentation, proportionality constants arrived at that provided a low level of error between the calculated curve and the manufacturer's curve (Figure 3). The following proportions showed an RMSE between the curves of 8.5 when using the $k - \varepsilon$ turbulence model:

$$Duct = 1.1 * Dvent \tag{9}$$

$$Length = 5.5 * Dvent \tag{10}$$

$$Sensor = \frac{Dvent}{6.65} \tag{11}$$

3.2 CFD Simulation Setup

To make the simulations as close to reality as possible, a wind tunnel was designed to calculate the characteristic curve of the fans to be used. The manufacturer's characteristic curve (pressure-flow ratio) for the analyzed commercial fan is adopted as a reference. This practice is consistent with recent literature (Ye et al., 2019) (Zhao et al., 2023) (Zhong et al., 2024). This work follows the same methodological approach. The manufacturer's curves, obtained on factory-certified test benches, are used as an external reference to adjust the virtual wind tunnel and calibrate the CFD–GA model. We are fully aware that this strategy does not replace experimental validation on a dedicated AMCA 210 test bench. Therefore, the results section reports percentage errors and adjustment metrics (RMSE) along the characteristic curve. The following experimental conditions are used for simulations:

Table 1. Environment and conditions used for simulations.

Category	Details
Hardware used	Ryzen 5 5600G
	32 GB RAM (2666 MHz)
Mesh type	Structured Cartesian immersed-body mesh
Number of cells	55215
Convergence criteria	0.5 Pa residual threshold
Configuration	Use current
Unit system	SI, angular velocity units: RPM
Analysis type	Internal
Fluid	Exclude cavities without flow conditions
Wall conditions	Gases / Air
Initial conditions	Default conditions
Boundary Conditions	Environment Pressure: 101325 Pa (293.2 K)
	Inlet Volume Flow: 0 - 0.1332083 m3/s
Internal Fan	Axial W4S200HH0401 230V/50Hz
Global Mesh	Level of initial mesh: 4
	With advanced channel refinement
Local Mesh	Fan fluid inlets and outlets

4 Results

The results are presented in three successive stages: Geometric sensitivity analysis of the virtual wind tunnel, (inferential statistical evaluation of the geometric parameters, and continuous optimization of the most critical parameter using a genetic algorithm, followed by CFD validation. Initially, various geometric configurations were simulated by modifying the proportional scaling factors of the tunnel diameter, tunnel length, and sensor positions. The resulting pressure-flow (P-Q) characteristic graphs were compared with manufacturer-certified data, and the error between the simulated and reference curves was quantified using MAPE and RMSE metrics (Fig. 3).

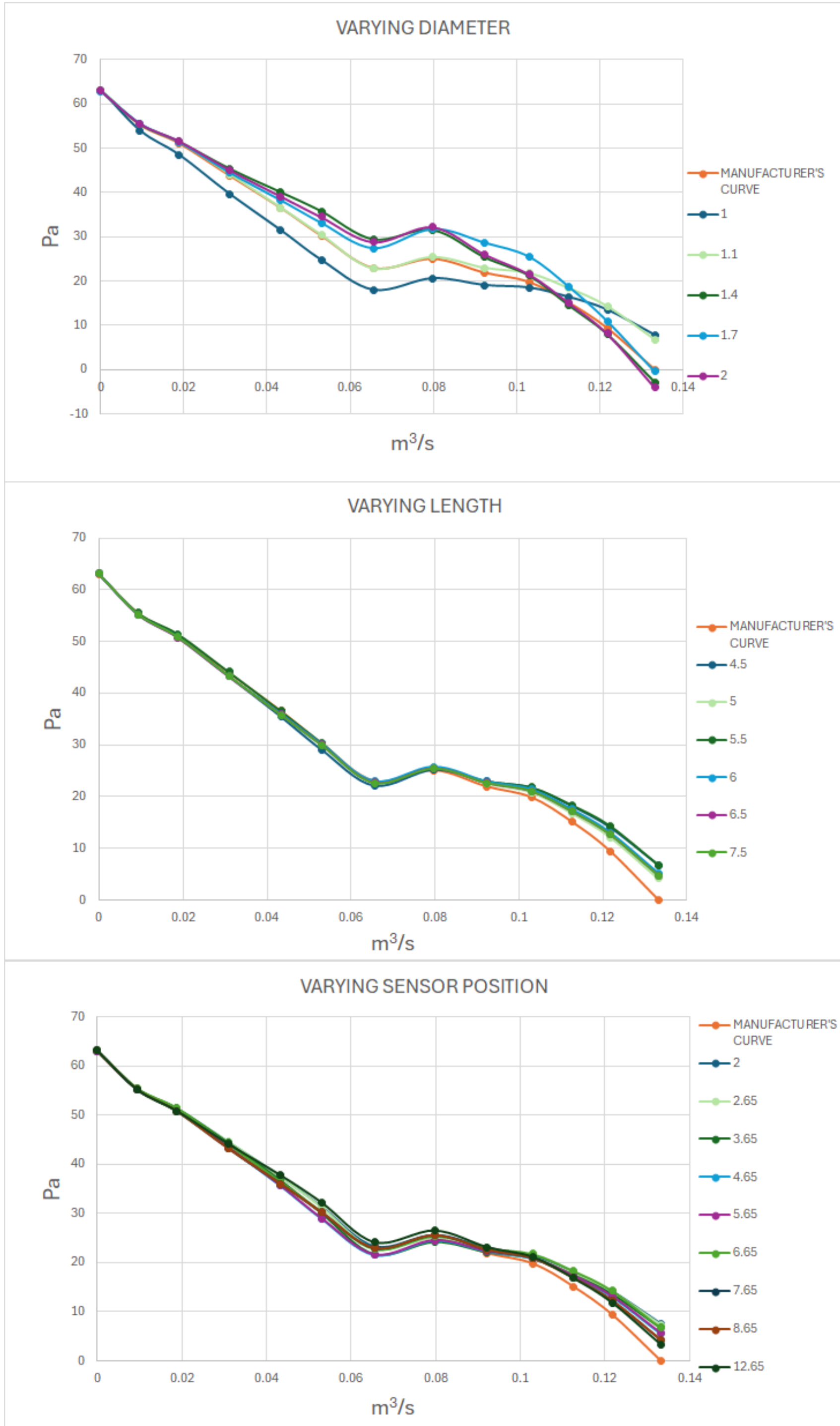

Fig. 3. Curves plotted by varying the wind tunnel dimensions.

Table 2 shows the pressure (Pa) values obtained for each proportional geometric configuration at all evaluated volumetric flow rates. Each "Curve" is related to a specific combination of scaling factors for sensor position, duct diameter, and tunnel length.. The column "CURVE" lists the different combinations used. In the columns "DUCT", "LENGTH" and "SENSOR" the proportionality constants for each tunnel dimension were placed. The group of columns entitled "VOLUME FLOW RATE" shows the different inlet flow rates with which the manufacturer's characteristic curve is plotted. The rows marked with yellow represent the values obtained that yielded the RMSE of 8.5 to make the variation of each value in each combination more visible.

Table 2. Curves calculated by varying the wind tunnel dimensions.

CURVE	DUCT	LENGTH	SENSOR	VOLUME FLOW RATE												
				0	0.0094622	0.0188364	0.0310278	0.0433222	0.0530389	0.0655778	0.0797667	0.0922167	0.1029528	0.1125639	0.12175	0.1332083
Curve 1	1	5.5	6.65	63.16	53.98	48.52	39.64	31.45	24.75	18	20.62	19.09	18.52	16.39	13.54	7.81
Curve 2	1.1	5.5	6.65	63.19	55.52	51.46	44.11	36.55	30.43	22.81	25.43	23	21.8	18.38	14.33	6.8
Curve 3	1.4	5.5	6.65	62.97	55.46	51.52	45.37	40.06	35.77	29.42	31.53	25.38	21.22	14.47	7.99	-2.88
Curve 4	1.7	5.5	6.65	62.84	55.48	51.33	44.43	38.2	33.14	27.45	31.76	28.7	25.53	18.73	11.02	-0.39
Curve 5	2	5.5	6.65	63.03	55.57	51.67	45.11	39.16	34.51	28.88	32.25	26.11	21.61	15.1	8.19	-3.98
Curve 6	1.1	4.5	6.65	63.1	55.2	50.9	43.22	35.47	29.06	22.08	25.17	22.91	21.68	18.17	13.99	6.73
Curve 7	1.1	5	6.65	63.17	55.23	50.78	43.26	36.18	30.37	23.02	25.63	22.59	20.85	16.84	12.16	4.16
Curve 8	1.1	5.5	6.65	63.19	55.52	51.46	44.11	36.55	30.43	22.81	25.43	23	21.8	18.38	14.33	6.8
Curve 9	1.1	6	6.65	63.17	55.24	50.87	43.25	36.05	30.23	22.99	25.78	22.93	21.4	17.53	13.02	5.14
Curve 10	1.1	6.5	6.65	63.17	55.23	50.8	43.23	35.92	30.05	22.73	25.51	22.68	21.09	17.19	12.67	4.78
Curve 11	1.1	7.5	6.65	63.1	55.23	50.86	43.27	35.81	29.92	22.6	25.4	22.64	21.05	17.14	12.62	4.71
Curve 12	1.1	5.5	2	63.14	55.31	51.29	44.52	37.45	31.34	23.27	25.59	22.93	21.33	17.78	14.1	7.54
Curve 13	1.1	5.5	2.65	63.14	55.35	51.33	44.56	37.46	31.24	22.8	25.08	22.56	21.04	17.76	14.04	7.35
Curve 14	1.1	5.5	3.65	63.14	55.43	51.42	44.35	36.76	30.07	21.72	24.24	22.16	20.87	17.52	13.62	6.72
Curve 15	1.1	5.5	4.65	63.12	55.19	50.93	43.38	35.64	28.98	21.6	24.55	22.32	20.91	17.31	13.1	5.63
Curve 16	1.1	5.5	5.65	63.11	55.19	50.91	43.38	35.64	28.98	21.6	24.54	22.3	20.91	17.31	13.1	5.64
Curve 17	1.1	5.5	6.65	63.19	55.52	51.46	44.11	36.55	30.43	22.81	25.43	23	21.8	18.38	14.33	6.8
Curve 18	1.1	5.5	7.65	63.16	55.23	50.8	43.23	36.07	30.25	22.95	25.58	22.62	20.9	16.92	12.28	4.31
Curve 19	1.1	5.5	8.65	63.15	55.23	50.81	43.22	36.07	30.25	22.95	25.59	22.62	20.9	16.92	12.28	4.31
Curve 20	1.1	5.5	12.65	63.14	55.2	50.84	44.12	37.78	32.21	24.11	26.5	23.13	21.14	16.82	11.82	3.33

However, to compare the results obtained with both turbulence models, it was decided to calculate the above combinations with the models provided by Flow Simulation. A comparison between the two models is shown in Figure 4.

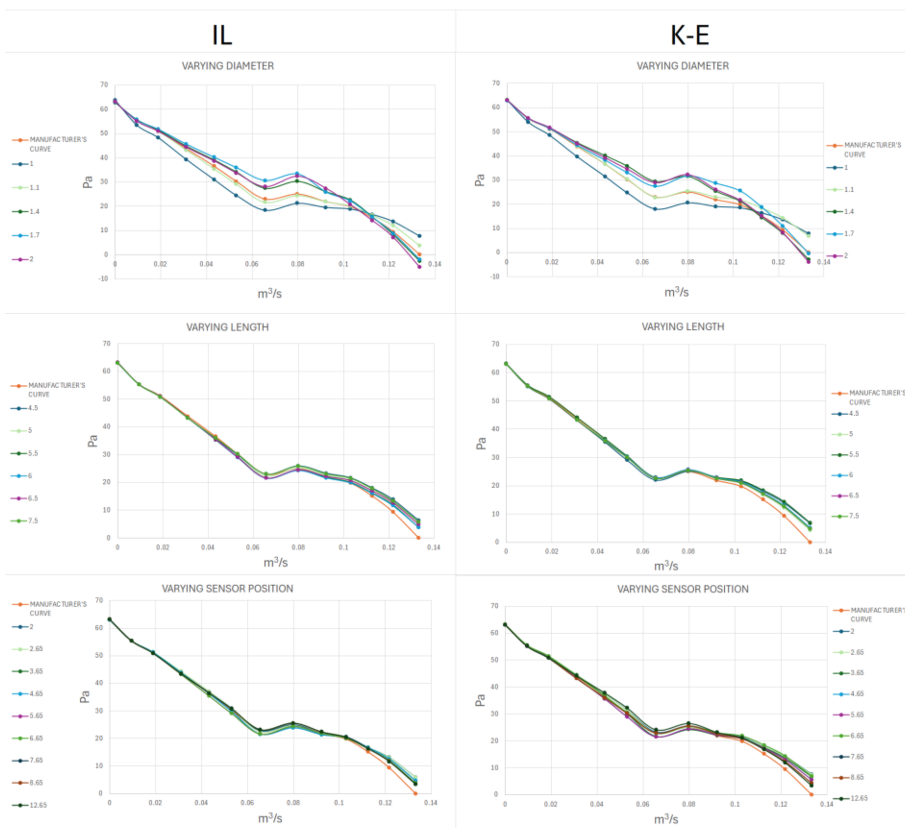

Fig. 4. Comparison of curves plotted with different Flow Simulation turbulence models.

When observing the sample curves obtained with both models, it can be noticed that the set of curves varying the sensor position shows smaller variation with the IL model than with the k-ε model. In contrast, for the set of curves varying the wind tunnel length, slightly smaller variation is observed with the k-ε model. In the case of the sets where the wind tunnel diameters were varied, larger variations are observed in both models compared to the other sets of the same turbulence model.

It was observed that the initial curve sample had a low population of curves obtained by modifying the diameter compared to the rest. It was decided to increase the sample size to perform a statistical analysis with similar population sizes, with the aim of balancing the sample sizes between the groups and allowing for a more robust statistical analysis. Table 3 expands the dataset used for statistical analysis, adding additional diameter configurations to balance group sizes and strengthen nonparametric tests.

Table 3. Sample curves used for statistical analysis.

CURVE	DUCT	LENGTH	SENSOR	VOLUME FLOW RATE												
				0	0.0094622	0.0188364	0.0310278	0.0433222	0.0530389	0.0655778	0.0797667	0.0922167	0.1029528	0.1125639	0.12175	0.1332083
Curve 1	1	5.5	6.65	63.16	53.98	48.52	39.64	31.45	24.75	18	20.62	19.09	18.52	16.39	13.54	7.81
Curve 2	1.05	5.5	6.65	63.21	54.71	49.72	41.55	33.95	27.9	20.93	23.58	21.19	19.85	16.48	12.49	5.36
Curve 3	1.06	5.5	6.65	63.22	54.84	50.02	41.97	34.49	28.49	21.43	24.05	21.56	20.14	16.62	12.46	4.94
Curve 4	1.08	5.5	6.65	63.17	55.06	50.48	42.67	35.31	29.42	22.19	24.86	22.17	20.63	16.89	12.51	4.68
Curve 5	1.1	5.5	6.65	63.19	55.52	51.46	44.11	36.55	30.43	22.81	25.43	23	21.8	18.38	14.33	6.8
Curve 6	1.17	5.5	6.65	63.11	55.58	51.53	44.65	37.99	32.56	25.16	27.78	24.21	22.09	17.46	12.02	2.74
Curve 7	1.4	5.5	6.65	62.97	55.46	51.52	45.37	40.06	35.77	29.42	31.53	25.38	21.22	14.47	7.99	-2.88
Curve 8	1.7	5.5	6.65	62.84	55.48	51.33	44.43	38.2	33.14	27.45	31.76	28.7	25.53	18.73	11.02	-0.39
Curve 9	2	5.5	6.65	63.03	55.57	51.67	45.11	39.16	34.51	28.88	32.25	26.11	21.61	15.1	8.19	-3.98
Curve 10	1.117	8.8	5	63.17	55.58	51.64	44.76	37.43	31.02	23.19	25.98	23.33	21.86	18.04	13.59	6
Curve 11	1.117	8.5	5	63.17	55.58	51.64	44.73	37.44	31.02	23.17	25.99	23.34	21.87	18.04	13.59	5.99
Curve 12	1.117	8.3	5	63.18	55.58	51.64	44.73	37.41	31.01	23.14	25.99	23.34	21.87	18.04	13.59	6
Curve 13	1.117	8	5	63.15	55.56	51.59	44.56	37.27	31.15	23.3	25.93	23.21	21.78	18.07	13.7	6.09
Curve 14	1.117	7.8	5	63.14	55.6	51.69	44.58	37.22	31.16	23.41	26.08	23.21	21.8	18.21	13.91	6.44
Curve 15	1.117	7.5	5	63.13	55.27	51.12	43.91	36.29	29.79	21.57	24.77	22.56	21.25	17.49	13.07	5.23
Curve 16	1.117	7.3	5	63.19	55.69	51.62	44.47	37.22	31.13	23.44	26.07	23.13	21.73	18.1	13.8	6.24
Curve 17	1.117	7	5	63.13	55.27	51.13	43.92	36.29	29.79	21.57	24.76	22.55	21.24	17.49	13.08	5.22
Curve 18	1.117	6.8	5	63.14	55.74	51.68	44.46	37.22	31.13	23.36	25.87	22.89	21.39	17.65	13.25	5.56
Curve 19	1.1	5.5	2	63.14	55.31	51.29	44.52	37.45	31.34	23.27	25.59	22.93	21.33	17.78	14.1	7.54
Curve 20	1.1	5.5	2.65	63.14	55.35	51.33	44.56	37.46	31.24	22.8	25.08	22.56	21.04	17.76	14.04	7.35
Curve 21	1.1	5.5	3.65	63.14	55.43	51.42	44.35	36.76	30.07	21.72	24.24	22.16	20.87	17.52	13.62	6.72
Curve 22	1.1	5.5	4.65	63.12	55.19	50.93	43.38	35.64	28.98	21.6	24.55	22.32	20.91	17.31	13.1	5.63
Curve 23	1.1	5.5	5.65	63.11	55.19	50.91	43.38	35.64	28.98	21.6	24.54	22.3	20.91	17.31	13.1	5.64
Curve 24	1.1	5.5	6.65	63.19	55.52	51.46	44.11	36.55	30.43	22.81	25.43	23	21.8	18.38	14.33	6.8
Curve 25	1.1	5.5	7.65	63.16	55.23	50.8	43.23	36.07	30.25	22.95	25.58	22.62	20.9	16.92	12.28	4.31
Curve 26	1.1	5.5	8.65	63.15	55.23	50.81	43.22	36.07	30.25	22.95	25.59	22.62	20.9	16.92	12.28	4.31
Curve 27	1.1	5.5	12.65	63.14	55.2	50.84	44.12	37.78	32.21	24.11	26.5	23.13	21.14	16.82	11.82	3.33

4.1 Statistical Analysis

After obtaining a sample of characteristic curves by modifying the wind tunnel dimensions, a statistical analysis was performed. This analysis evaluated whether the three geometric variables (diameter, length, and sensor position) were determining factors in calculation accuracy.
To avoid overestimating large measurement errors and underestimating small ones, the errors obtained for the evaluated configurations were used directly, focusing on central tendency and dispersion.

The simple error between each pressure value of the simulated curves and the target curve was used to analyze bias, and dispersion was evaluated using the variance of the error. The use of the average error maintains the direction of the bias and avoids the artificial reweighting of extreme values. This approach is more suitable for stability and sensitivity analysis in CFD simulations with non-normal distributions.

The statistical analysis was performed with a significance level of $\alpha=0.05$. An analysis of variance was proposed on the error values associated with the curves obtained by varying each geometric parameter. For each geometric parameter, assumptions of normality and homogeneity of variances were evaluated. Measures of central tendency were also compared.

Sample analysis with diameter variation. When performing the test for equality of variances in the sample with diameter variation in the wind tunnel, Levene's test yielded a value of $p=0.050$ and $p=0.030$ through multiple comparisons. Therefore, the null hypothesis of equality of variances is rejected, obtaining evidence that at least one variance is different from the rest. In the case of normality, the Anderson-Darling (A-D) test was used on the error sets corresponding to each diameter configuration. The results showed that some samples did not reject normality, while others did show statistical evidence against it. This indicates that the error distribution depends on tunnel diameter value. Analysis of normal probability plots in the residuals of the samples with diameter variation revealed systematic curvatures with respect to the straight line, deviations in the tails, and asymmetric accumulation of points. These results indicate asymmetrical and violation of the normality assumption.

The non-viability of applying Welch's ANOVA was verified by performing it and subsequently verifying the assumptions of normality and homoscedasticity through residual analysis. Since the residuals did not meet the normality assumption, nonparametric tests were performed on the measurement errors corresponding to each geometric configuration. For this purpose, the Kruskal-Wallis test was used to compare medians, with a significant level of 0.05, obtaining a value of $p=0.98$. Thus, the null hypothesis of equality of medians is not rejected, and there is no evidence to suggest the existence of statistically significant differences between medians.

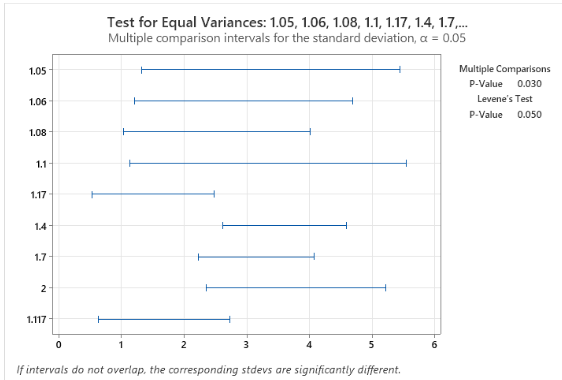

Fig. 5. Test for equal variances with diameter variation.

Sample analysis with length variation. These tests were replicated with the curve samples obtained by varying the length of the wind tunnel. The variance comparison test reported a p-value of 1 using both the Levene test and multiple comparisons. Thus, the null hypothesis of equal variances is not rejected, and the variances are considered equal. Anderson-Darling test results for samples with tunnel length variation showed that some samples did not reject normality, while others showed evidence against it. Given the absence of normality, a nonparametric approach was preferred.

Using the Kruskal-Wallis test on the residuals of the sample curve obtained by varying the length of the wind tunnel, a value of p=1 was obtained. The null hypothesis of equality of medians is not rejected, so no statistically significant differences between medians are detected.

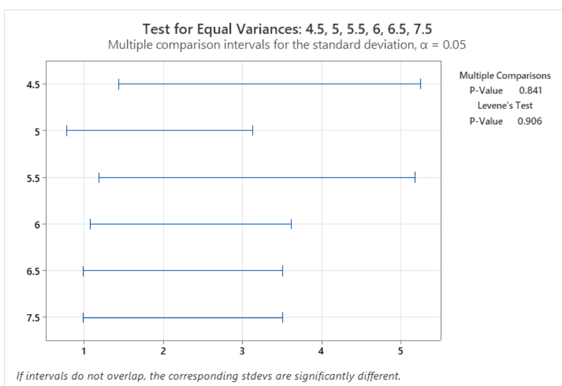

Fig. 6. Test for equal variances with length variation.

Sample analysis with variation in the position of the pressure sensors. Finally, the same tests were performed on the sample of curves obtained by varying the position of the pressure sensors. Levene's test yielded p = 0.982, with no evidence of differences between variances. Thus, the null hypothesis of homoscedasticity is not rejected because no statistically significant differences between variances are detected.

A-D test results for samples with variation in the position of the wind tunnel sensors showed that some samples did not reject normality, while others showed evidence against it. Therefore, normality of residuals cannot be assumed. Given the absence of normality, the use of a classical parametric ANOVA is not appropriate, and a non-parametric approach is chosen. Using the Kruskal-Wallis test on the residuals of the sample of curves obtained by varying the position of the wind tunnel sensors, a value of p=0.917 was obtained. The equality of medians is not rejected since no statistically significant differences are detected.

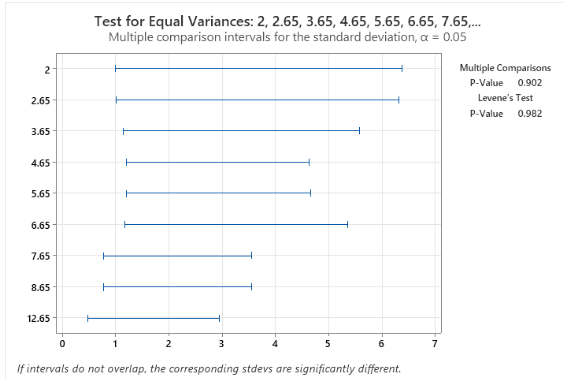

Fig. 7. Test for equal variances with variation in the position of pressure sensors.

Table 4 summarizes the inferential statistical results obtained from Levene's test, Anderson–Darling normality assessment, and Kruskal–Wallis median comparison for each geometric parameter.

Table 4. Summary of the results obtained in the statistical analysis.

	Diameter	Length	Pos. Sens.
Variance	Significant differences	No significant differences	No significant differences
Median	No significant differences	No significant differences	No significant differences
Normality	Not consistent	Not consistent	Not consistent
Effect on accuracy of the simulated curve	Detected	Not detected	Not detected

Table 5 reports descriptive RMSE statistics (mean, standard deviation, minimum, and maximum) for each geometric parameter group, allowing comparison of dispersion trends observed in the dataset.

Table 5. Summary of RMSE statistics for geometric parameter variation.

Parameter Varied	Number of Configurations	Mean NRMSE (%)	Standard Deviation (%)	Minimum NRMSE (%)	Maximum NRMSE (%)
Diameter	10	8.82	8.05	5.27	13.43
Length	10	6.11	6.30	5.87	7.75
Sensor Position	9	5.09	4.61	3.95	6.71

Statistical analysis indicates that diameter is a geometric parameter that affects the accuracy of the characteristic curve calculation. Although it is visually apparent that diameter is a parameter that significantly affects the accuracy of the simulated characteristic curve, this is supported by the statistical analyses performed. So why are the characteristic curves simulated with different sensor length and position values not the same? To explain this, we need to analyze the calculation methodology used by the Solidworks Flow Simulation module.

During simulation, Flow Simulation performs iterative solutions of the Navier-Stokes equations. During these iterations, the solver will decrease the margin of error between values. By default, Solidworks defines a maximum margin of error for each simulation, but the user can define this value manually. For all characteristic curve simulations, a maximum margin of error of 0.5 Pa was used, although all values obtained margins of error much lower than this. It is difficult to achieve exact convergence in all target variables. However, the variability of convergence errors associated with each pressure value was not analyzed. These differences in errors may explain the subtle variations between curves but are not considered determining factors affecting accuracy of the simulated characteristic curves.

4.2 Genetic Algorithm

Once the sample curves had been defined, which would be those obtained using the k-ε model, a genetic algorithm was used to optimize an objective function defined as the quadratic error between the interpolated flow values and the target values. The pipe diameter was selected as the optimization variable due to its observed influence on the characteristic curve behavior and its importance as a primary geometric parameter of the system.

This methodology allows replicating the procedure in similar applications that require the optimization of continuous parameters by means of genetic algorithms. Such implementation was carried out by means of the DEAP library, providing flexibility in the configuration of the genetic operators and the handling of continuous individuals.

While Table 6 details the procedural steps of the Genetic Algorithm (GA) methodology, the resulting operational specifications are presented below. Table 7 summarizes the main technical and methodological aspects of a genetic algorithm designed to optimize the diameter in a flow system. The key parameters, the methods employed and the advantages and disadvantages of the approach are detailed, facilitating its application in similar optimization problems. The use of a genetic algorithm allows the entire parameter space to be explored, discarding local minimum and finding optimal geometric configurations that reduce the RMSE.

Table 6. Genetic Algorithm Methodology

Phase	Description	Technical Details
Loading and preprocessing of experimental data	Data were loaded from a CSV file with flow and diameter values using pandas and numpy. The flow columns were processed to obtain the required numerical values.	Libraries: pandas, numpy. Input: CSV file. Processing: selection of flow columns.
Data interpolation	Linear interpolation (interp1d) was used to generate intermediate flow values over a continuous range of diameters with 0.001 resolution.	Tool: scipy.interpolate.interp1d. Generated range: [1.0, 2.0] with 0.001 increment.
Definition of objective function	The objective function was defined as the quadratic error between interpolated values and target-predefined values, penalizing solutions outside the range.	Metric: sum of squared errors between interpolated and target values. Penalty for out-of-range values: high.
Genetic Algorithm Configuration	It was implemented using the DEAP library, defining individuals as continuous diameters within the range [1.0, 2.0], with tournament selection, blend crossover, and Gaussian mutation.	Library: DEAP. Operators: tournament selection (size 3), blend crossover (α=0.5), Gaussian mutation (μ=0, σ=0.001).
Genetic Algorithm Execution	The GA evolved over 100 generations with crossover (50%) and mutation (20%) probabilities, recording results per generation.	Initial population: 50 individuals. Evolution: 100 generations. Probabilities: crossover 50%, mutation 20%.
Analysis and Visualization of Results	The optimal diameter was identified by comparing obtained and expected flow values, and fitness, diameter, and error graphs were analyzed.	Tools: matplotlib. Outputs: fitness graphs by generation, flow comparison, and diameter-fitness relationship.

Table 7 provides computational specifications, evolutionary operators, genetic representation, and optimization parameters used in the GA implementation.

Table 7. Details of the genetic algorithm.

Category	Details
Programming language	Python
Libraries	scipy, numpy, pandas, deap

Computational environment	Windows 10 Pro Version 22H2 Processor: AMD Ryzen 5 5600G with Radeon Graphics 3.90 GHz Installed RAM: 32.0 GB (31.8 GB usable) Storage: 932 GB SSD CT1000MX500SSD1, 932 GB HDD TOSHIBA MQ01ABD100 Graphics card: NVIDIA GeForce RTX 3060 (12 GB) System type: 64-bit operating system, x64 processor
Type of Representation	Genotype represented as a float value encoding diameter; phenotype corresponds to interpolated flow values associated with diameter.
Selection	Tournament selection with tournament size of 3. This method ensures balanced selective pressure by selecting the best of three random individuals.
Mutation	Gaussian mutation with mean (mu) of 0, standard deviation (sigma) of 0.001 and individual probability (indpb) of mutation of 20%. Introduces variation to avoid stagnation.
Mutation percentage	Overall probability of 20% of applying mutation to an individual in each generation.
Special Operators	Blend cross (cxBlend) with alpha parameter of 0.5, which generates offspring as an even mixture of the two parents.
Objective Function	Minimizes the squared error between interpolated flow values and expected target values: [Fitness=∑(interpolated_values - target values)^2]. High penalty (1e6) for diameters outside the interpolated range.
Individuals	Initial population composed of 50 individuals.
Generations	100 generations, ensuring a balance between exploration and exploitation of the search space.
Genetic Coding	- Genotype: List of length 1 with a single float value. - Phenotype: Interpolated flow values calculated for the corresponding diameter.
Execution	- Initialization: Random generation of diameters between 1.0 and 2.0. - Evaluation: Calculation of fitness for each individual. - Reproduction: Application of crossing and mutation. - Selection: Preservation of the best individuals in each generation.
Visualization and Results	Detailed graphs and analysis: - Fitness evolution over generations. - Comparison of target values vs. obtained values. - Relationship between diameter and fitness.
Advantages	- Effective in non-linear problems with multiple local optima. - Easy interpretation of results. - Adaptable to various optimization problems.
Disadvantages	- Dependence on key parameters such as population size, generations and crossover/mutation probabilities. - High computational cost in more complex or dimensional problems.

4.3 Post-Optimization CFD Validation

Using the genetic algorithm, it was determined that the pipe diameter providing the best results is $Ducto = 1.19 * Dvent$. So, the next step would be to vary again the values of the length and distance of the sensors to find a curve with an RMSE less than 8.5. Although length did not prove to be a significant parameter for accuracy between the target curve and the simulated curve in the statistical analysis, this parameter was adjusted to the value that provided the lowest RMSE.

By varying only, the length of the tunnel, it was observed that with the constant of 7.5, the RMSE was reduced to 5.5. Once the tunnel length value that allowed for a reduction in the RMSE was found, the variation in sensor distance was continued. Finally, when calculating the RMSE of the last curves, the value was reduced from 5.5 to 5.2 with a constant of 5 in the sensor distance. The comparison between these curves is shown in Figure 8. Based on sensitivity analysis and optimization using genetic algorithms, a geometric combination was selected that offers the best compromise between precision and robustness:

$$Duct = 1.19 * Dvent \tag{12}$$

$$Length = 7.5 * Dvent \tag{13}$$

$$Sensor = \frac{Dvent}{5} \tag{14}$$

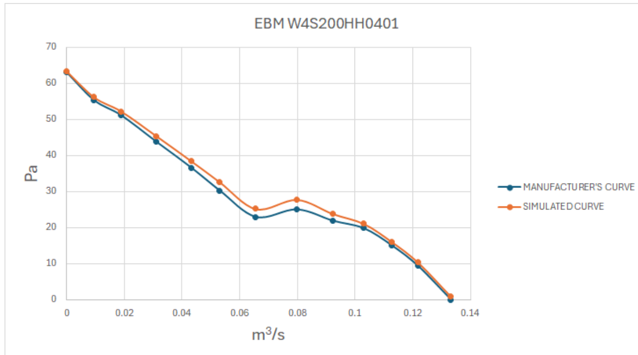

Fig. 8. Comparison between characteristic curves after optimizing wind tunnel measurements.

Tables 8, 9, and 10 present the parametric analysis of the model's performance using the mean absolute percentage error (MAPE) and its coefficient of variation, considering different duct diameters, duct lengths, and sensor positions, respectively. These results allow evaluating the sensitivity of the model to variations in each analyzed geometric and operational parameter.

Table 8 shows that the MAPE varies considerably with duct diameter, reaching minimum values close to 4.50% and maximum values above 60%, indicating that diameter has a significant influence on model accuracy.

Table 8. Effect of duct diameter scaling factor on MAPE and MAPE coefficient of variation

		DUCT
Value	MAPE	MAPE coefficient of variation
1	60.0397598	74.3826839
1.05	15.7623999	87.1237353
1.06	11.1583846	98.297291
1.08	6.90867766	144.906595
1.1	12.7271701	182.32258
1.117	4.50092881	140.603507
1.17	11.9604649	65.2940405
1.19	10.6037652	78.4294011
1.4	47.3357488	135.36966
1.7	43.0783805	123.624632
2	43.5798156	137.525373

On the other hand, Table 9 shows that, for different duct lengths, the MAPE remains within a smaller range, approximately between 5.60% and 11.80%, indicating that the model is less sensitive to this parameter compared to diameter.

Table 9. Effect of duct length scaling factor on MAPE and MAPE coefficient of variation

		LENGTH
Value	MAPE	MAPE coefficient of variation
4	7.13067354	168.055875
4.5	6.64098757	162.441153
5	6.22942291	174.008927
5.5	6.93759999	171.624848
6	10.7721488	169.075248
6.3	5.59856993	172.709401
6.5	9.12152726	172.22858

6.8	9.23193097	158.024634
7	7.86831112	169.247434
7.3	11.7955908	157.918653
7.5	7.87742117	169.344039

Finally, Table 10 presents the results corresponding to variation in sensor position, where the lowest MAPE values are observed, with minimum values close to 2.81%, indicating that certain sensor positions allow greater accuracy in the model predictions.

Table 10. Effect of sensor position scaling factor on MAPE and MAPE coefficient of variation

	SENSOR	
Value	MAPE	MAPE coefficient of variation
2	7.70164048	221.10082
2.65	7.49622909	219.527165
3.65	5.86425157	170.513065
4.65	5.90268041	170.632513
5.65	5.00933827	133.234188
6.65	4.97805121	133.417248
7.65	2.81131097	189.224487
8.65	2.81756802	189.064488
12.65	2.81131097	189.224487

The next step was to check that the wind tunnel design would be functional for fans of different sizes, which would also have different maximum operating speeds as can be seen in figure 9.

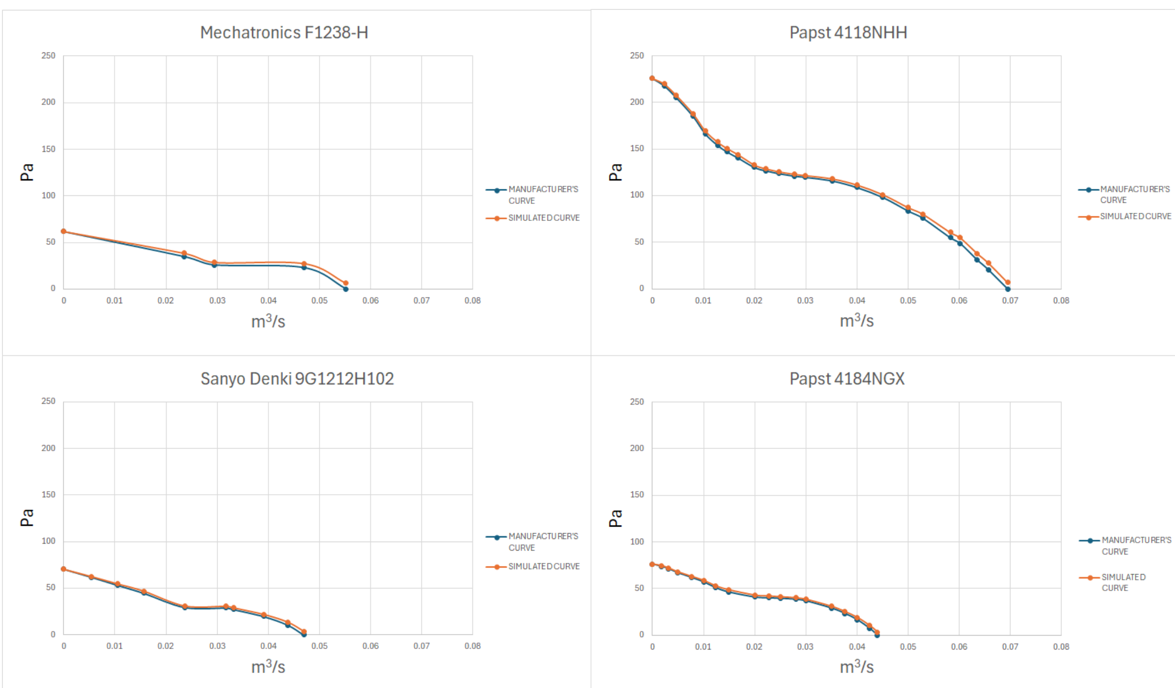

Fig. 9. Comparison between characteristic curves for different fans.

After verifying that this combination not only produces the lowest error for the reference fan but also proved to be scalable to fans of different diameters and operating speeds, maintaining errors below 10% in the simulated characteristic curves, the last step would be to calculate the curve of a fan simulated as a rotating element. For this purpose, a fan was designed as similar as possible to the commercial fan. This 120 mm fan model was selected because it is used for cooling the internal components of a computer in addition to the fact that the manufacturer adds the characteristic curve, which is uncommon for fans of this type. This allows a direct comparison between the theoretical and simulated curves obtained in the tunnel.

Finally, based on descriptive dispersion trends and aerodynamic confinement considerations, a genetic algorithm was implemented to perform continuous optimization of the selected geometric parameter (Fig. 11). The optimized configuration was then validated through additional CFD simulations and comparative analysis against experimental reference curves.

Fig. 10. Comparison between the real model and the model used for the simulations of the commercial fan.

The model of the fan used is shown in Figure 10, as well as the fan inserted in the tunnel of the corresponding size following the previously calculated constants (Figure 11).

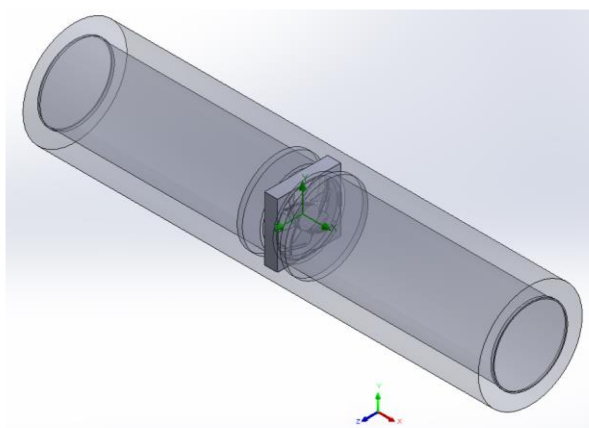

Fig. 11. Fan model and its respective wind tunnel used for simulations.

The adaptive refinement offered by SOLIDWORKS Flow Simulation was used for the mechanical simulation of the fan model. This decision was made because, when performing the simulation with a local rotating region with local mesh refinements, the variation of the data value was high compared to simulations without rotating region even though a steady state rotation approach was considered where the values in the rotating region are averaged. Once the fan was properly simulated the pressure differences were recorded for the same flow rates as provided by the manufacturer, the following illustration shows this comparison (Figure 12):

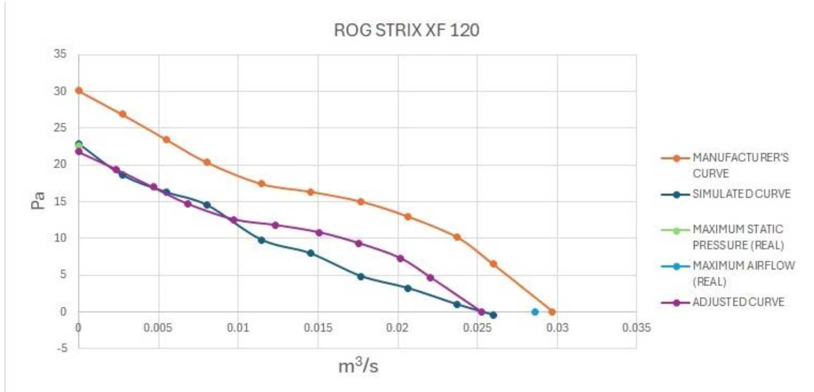

Fig. 12. Comparison between experimental, theoretical and calculated values of the commercial fan.

As observed, a larger discrepancy exists between these curves. This difference can be primarily attributed to design-related factors. Although the virtual model was constructed to replicate the real fan as closely as possible, certain geometric parameters—such as blade curvature and detailed aerodynamic profiles—are inherently difficult to reproduce with complete accuracy in a CFD-based reconstruction. Furthermore, a technical review published on HWCooling (2022) provides an independent performance assessment of the commercial fan model. In that review, the measured maximum airflow and static pressure values are compared against the manufacturer's theoretical specifications, revealing observable deviations between rated and experimentally obtained performance. These findings are consistent with the discrepancies identified in the present study.

With this data it is verified that the fan does not reach the maximum values set by the manufacturer, obtaining a real maximum static pressure of 74.7% of the theoretical one, while the real maximum flow rate reaches 96.2% of the theoretical one. Taking these real maximum values as a reference for comparison with those obtained in the simulation, we find an RMSE of 1.7 for the maximum static pressure and 9.2 for the maximum flow rate. Since the RMSE in both values is less than 10, the values can be taken as reliable. Figure 12 shows the actual maximum values provided by HWCooling (2022) in addition to the manufacturer's curve, adjusted to 85%.

In this last comparison of the curves, discrepancies between certified and independently measured maximum values were observed at least at the maximum points of flow and static pressure since the adjusted curve only passes through one of these points at a time (Figure 13). In addition, there is a difference between the simulated curve and the fitted curve that can be explained by the airfoil used in the actual design and the one used for the simulations. When comparing the adjusted simulated curve, a RMSE of 2.33 is obtained. According to (Corsair, 2024), the shape of the blades, casing and even the material are factors that affect the performance of a fan, so the fan design process tends to be lengthy to achieve optimal performance.

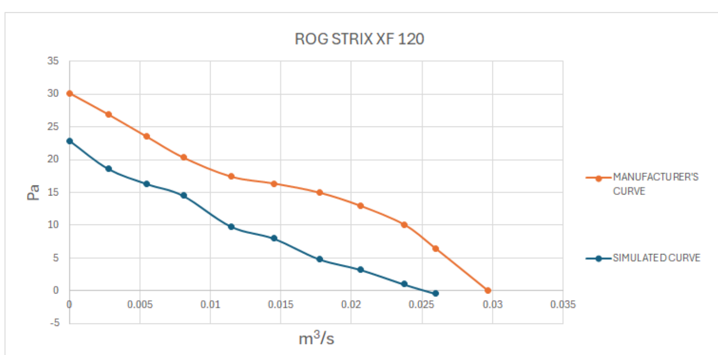

Fig. 13. Characteristic curve given by the manufacturer compared with the characteristic curve obtained in simulations.

5 Discussion

Inferential statistical tests (Anderson–Darling, Levene's test, and Kruskal–Wallis) did not detect statistically significant differences in median error among the discrete geometric configurations within the proportional ranges evaluated ($p > 0.05$). Therefore, no distributional shift in median error could be established through hypothesis testing alone.

However, descriptive RMSE analysis showed comparatively higher dispersion when varying tunnel diameter. Based on this observed trend and aerodynamic confinement considerations, diameter was selected for continuous optimization using a genetic algorithm (Moradihaji et al., 2024). The evolutionary optimization procedure directly minimized RMSE without replacing CFD physics with surrogate models. The optimized tunnel geometry reduced the discrepancy between simulated and certified curves to below 10% error, indicating that geometric calibration of the simulation domain can improve agreement with experimental reference data.

Validation using an independent fan model confirmed that the optimized geometry generalizes beyond the calibration case, supporting the robustness of the proposed framework. Overall, these findings demonstrate that evolutionary optimization can be effectively used not only for blade design but also for calibration of computational test environments, preserving physical interpretability while improving numerical–experimental consistency.

Although significant progress has been made in recent years in the simulation and characterization of axial fans using CFD, research has mainly focused on impeller geometry and aerodynamic optimization of blades or guide elements. For example, Wang & Kruyt (2020) validated CFD models for low-pressure fans through direct comparison with experimental measurements, while Szelka et al. (2023) investigated the effects of blade aerodynamic profile and skew using CFD and physical prototyping. Similarly, Zhou et al. (2023) employed multi-objective genetic algorithms (NSGA-II) to optimize guide vane geometry in large-scale fans. Other studies have also demonstrated the effectiveness of evolutionary optimization in aerodynamic applications. Likewise, Radi et al. (2023) applied genetic algorithms combined with the XFOIL solver to design wind turbine airfoils, obtaining optimized geometries that improved aerodynamic performance.

However, no recent study explores the virtual wind tunnel itself as an object of optimization, where its dimensions are used as calibration variables to minimize the error between CFD simulations and certified manufacturer curves, nor integrates this calibration approach with genetic algorithms specifically applied to low-pressure PC fans.

The results obtained with the proposed methodology show high reliability, with error margins below 10%. In comparison, Hirano et al. (2017) reported discrepancies between experimental and simulated characteristic curves typically exceeding 20%, with only one case achieving approximately 13% error. These differences highlight the importance of proper calibration and modeling conditions. While previous studies have shown that blade geometry strongly influences fan performance, the present results demonstrate that optimization of the computational test environment itself represents an additional and effective strategy to improve CFD accuracy.

6 Conclusions

Descriptive analysis suggests greater sensitivity of the simulated characteristic curve. Based on statistical and RMSE analysis, a genetic algorithm was applied to optimize this parameter, while the remaining geometric parameters were not selected for continuous optimization due to their lower sensitivity within the evaluated ranges.

Although the tests carried out show that the length and position of the sensors in the wind tunnel do not affect the accuracy of the simulated curves, these tests do not rule out the possibility that these values may affect accuracy in the simulated characteristic curve in ranges higher than those analyzed here. Therefore, if the wind tunnel has sensor length and positioning values within the ranges simulated above, the error in the curve obtained will not increase significantly. These findings are consistent with the Kruskal–Wallis and Levene's tests, which confirmed no statistically significant effect of tunnel length or sensor position on error magnitude or variance.

This study does not seek to replace or compete with the methodology proposed by AMCA Sandard 210. As part of the future work, the wind tunnel design will be implemented to compare the experimental and calculated results, as well as to compare the experimental results of the proposed design with those obtained in the wind tunnel, as established by the AMCA 210 standard.

Instead, it proposes a complementary computational calibration approach to improve agreement between CFD simulations and certified manufacturer data.

At this stage, direct experimental validation is not yet possible due to the absence of an AMCA-compliant facility, whose design and implementation require substantial infrastructure and investment. However, the present results establish a solid computational foundation for future experimental verification and practical implementation.

References

Ahmed, D. E., & Eljack, E. M. (2014). Optimization of model wind-tunnel contraction using CFD. In J. P. Meyer (Ed.), *Proceedings of the 10th International Conference on Heat Transfer, Fluid Mechanics and Thermodynamics* (pp. 87–92). https://hdl.handle.net/2263/44511

Fritsche, M., & Epple, P. (2025). AI-prediction of pressure characteristics for centrifugal fans. In *Proceedings of the ASME 2025 Fluids Engineering Division Summer Meeting* (Vol. 2, Article V002T08A005). American Society of Mechanical Engineers. https://doi.org/10.1115/FEDSM2025-156474

Hirano, T., Takahashi, K., & Minorikawa, G. (2017). Study on performance evaluation of small axial fan. *Open Journal of Fluid Dynamics, 7*(4), 546–556. https://doi.org/10.4236/ojfd.2017.74037

Kumar, A., Manas, M. P., & Pradeep, A. M. (2022). Identification and classification of operating flow regimes and prediction of stall in a contra-rotating axial fan using machine learning. *The Aeronautical Journal, 126*(1302), 1351–1369. https://doi.org/10.1017/aer.2022.63

Launder, B. E., & Spalding, D. B. (1974). The numerical computation of turbulent flows. *Computer Methods in Applied Mechanics and Engineering, 3*(2), 269–289. https://doi.org/10.1016/0045-7825(74)90029-2

Liu, Y.-L., Nisa, E. C., Kuan, Y.-D., Luo, W.-J., & Feng, C.-C. (2023). Combining deep neural network with genetic algorithm for axial flow fan design and development. *Processes, 11*(1), Article 122. https://doi.org/10.3390/pr11010122

Moradihaji, K., Ghassemi, M., & Pourbagian, M. (2024). Off-design performance analysis of a radial fan using experimental, computational, and artificial intelligence approaches. *European Journal of Mechanics—B/Fluids, 104*, 150–172. https://doi.org/10.1016/j.euromechflu.2023.12.005

Radi, J., Djebli, A., Sierra-García, J. E., & Santos, M. (2023). Diseño de formas aerodinámicas de las palas de aerogeneradores mediante algoritmos genéticos: Una primera aproximación. In *XLIV Jornadas de Automática: Libro de actas* (pp. 12–16). Servizo de Publicacións da Universidade da Coruña. https://doi.org/10.17979/spudc.9788497498609.012

Samák, Ľ. (2022, January 7). *Asus ROG Strix XF120: An excellent fan, but only in some ways*. HWCooling. https://www.hwcooling.net/en/asus-rog-strix-xf120-an-excellent-fan-but-only-in-some-ways/

Szelka, M., Drwięga, A., Tokarczyk, J., Szyguła, M., Szewerda, K., Banaś, M., Kołodziejczyk, K., & Kędzia, K. (2023). Study of the blade shape impact on the improvement of fan efficiency based on state-of-the-art prototyping methods. *Energies, 16*(1), Article 542. https://doi.org/10.3390/en16010542

Wang, J., & Kruyt, N. P. (2020). Computational fluid dynamics simulations of aerodynamic performance of low-pressure axial fans with small hub-to-tip diameter ratio. *Journal of Fluids Engineering, 142*(9), Article 091202. https://doi.org/10.1115/1.4047120

Ye, X., Fan, F., Zhang, R., & Li, C. (2019). Prediction of performance of a variable-pitch axial fan with forward-skewed blades. *Energies, 12*(12), Article 2353. https://doi.org/10.3390/en12122353

Zhang, Y., Wang, Y., & Li, J. (2019). Volume flow rate optimization of an axial fan by artificial neural network and genetic algorithm. *Open Journal of Fluid Dynamics, 9*(3), 207–223. https://doi.org/10.4236/ojfd.2019.93014

Zhao, W., Wasala, S., & Persoons, T. (2023, June 13). *Rapid and accurate analytical model for predicting axial fan performance in electronics cooling*. Electronics Cooling. https://www.electronics-cooling.com/2023/06/rapid-and-accurate-analytical-model-for-predicting-axial-fan-performance-in-electronics-cooling/

Zhong, Y., Xu, W., & Shi, Y. (2026). Flow characteristics and thermal fields in fan-coupled jet impingement. *Numerical Heat Transfer, Part A: Applications, 87*(1), 1–19. https://doi.org/10.1080/10407782.2024.2390683

Zhou, S., Zhang, T., Mao, Z., & Lu, L. (2023). Multi-objective optimization of an IGV for a large axial fan based on NSGA-II. *Frontiers in Energy Research, 10*, Article 994654. https://doi.org/10.3389/fenrg.2022.994654